Inorganic Chemistry

ARTICLE

pubs.acs.org/IC

Optical and Photocatalytic Properties of Heavily F^--Doped SnO_2 Nanocrystals by a Novel Single-Source Precursor Approach

Vinod Kumar,[†] A. Govind,[‡] and R. Nagarajan*,[†]

[†]Materials Chemistry Group, Department of Chemistry, University of Delhi, Delhi 110 007, India

[‡]Physics of Energy Harvesting, National Physical Laboratory (CSIR), Dr. K.S. Krishnan Marg, New Delhi-110 012, India

Supporting Information

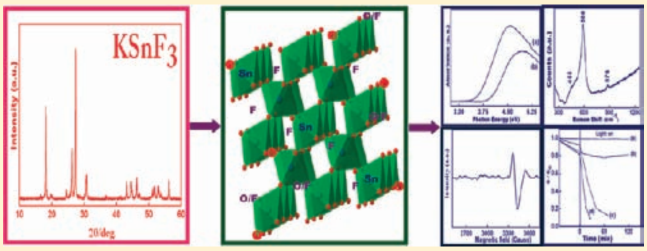

ABSTRACT: Heavily F-doped SnO_2 nanocrystals were successfully prepared by a novel synthetic approach involving low-temperature oxidation of a Sn^{2+}-containing fluoride complex $KSnF_3$ as the single-source precursor with H_2O_2. The F-doped SnO_2 powder was characterized by powder X-ray diffraction, TG-MS, BET surface area, diffuse reflectance spectroscopy, XPS, PL, FTIR spectroscopy, Raman spectroscopy, EPR spectroscopy, SEM, and TEM. Broadening of the diffracted peaks, signifying the low crystallite size of the products, was quite evident in the powder X-ray diffraction pattern of SnO_2 obtained from $KSnF_3$. It was indexed in a tetragonal unit cell with lattice constants $a = 4.7106$ (1) Å and $c = 3.1970$ (1) Å. Agglomeration of particles, with an average diameter of 5−7 nm, was observed in the TEM images whose spotwise EDX analysis indicated the presence of fluoride ions. In the core level high-resolution F 1s spectrum, the peak observed at 685.08 eV was fitted by the Gaussian profile yielding the fluoride ion concentration to be 21.23% in the SnO_2 lattice. Such a high fluoride ion concentration is reported for the first time in powders. SnO_2:F nanocrystals showed greater thermal stability up to 300 °C when heated in a thermobalance under flowing helium, after which generation of small quantities of HF was observed in the TG coupled mass spectrometry analysis. The band gap value, estimated from the Kubelka−Munk function, showed a large shift from 3.52 to 3.87 eV on fluoride ion doping, as observed in the diffuse reflectance spectrum. Such a large shift was corroborated to the overdoped situation due to the Moss−Burstein effect with an increase in the carrier concentration. In the photoluminescence (PL) spectrum, SnO_2:F nanocrystals exhibited a broad green emission arising from the singly ionized oxygen vacancies created due to higher dopant concentration. The evidence for singly ionized vacancies was arrived from the presence of a signal with a g value of 1.98 in the ESR spectrum of SnO_2:F at room temperature. The disordered nature of the rutile lattice and the enormous oxygen vacancies created due to fluoride ion doping were evident from the broad bands observed at 455, 588, and 874 cm^{-1} in the room-temperature Raman spectrum of SnO_2:F. As the consequence of the oxygen vacancies, F-doped SnO_2 was examined for the function as a photocatalyst in the degradation of aqueous RhB dye solution under UV irradiation. A very high photocatalytic efficiency was observed for the F-doped SnO_2 nanocrystals as compared to pure SnO_2. The BET surface area of pure SnO_2 was quite high (207.81 m^2/g) as compared to the F-doped SnO_2 nanocrystals (45.16 m^2/g). Pore size analysis showed a mean pore diameter of 1.97 and 13.97 nm for the pure and doped samples. The increased photocatalytic efficiency was related to the very high concentration of oxygen vacancies in SnO_2 induced by F doping.

1. INTRODUCTION

In the field of advanced materials, nanocrystals have been widely investigated to explore their unusual properties for a variety of applications.[1−4] Even more interesting phenomena are expected for the doped nanocrystals. In recent years, there has been increased interest in doped metal oxide nanocrystals because of their diverse industrial applications in electrochromic devices,[5] lasers,[6] transparent conductors,[7,8] gas sensors,[9,10] light-emitting devices,[11] photonic crystals,[12] fluorescent materials,[13] heat reflectors and solar cell panels,[14] photocatalyst,[15] electrochemical oxidation,[16] lithium-ion battery electrode,[17,18] spintronics applications,[19] and superconductors.[20]

Anionic doping, especially fluoride-ion doping, has attracted a lot of attention from researchers to engineer the band gap and to modify the optical properties of metal oxides due to the similar ionic size of F^- and O^{2-} . SnO_2 has been the leading candidate among the extensively investigated transparent conducting oxides (TCO) for a variety of reasons.[7] It is a n-type wide band gap semiconductor showing high chemical and mechanical stabilities with unique photoelectronic properties.[7] SnO_2 has additional applications as gas sensors and as an oxide matrix in the dye-sensitized solar cells.[21] The possible use of SnO_2 as an alternative to graphite in Li-ion batteries using a graphite anode has also been studied due to its high specific capacity.[18] Doping with a Cl, Sb, Mo, or F atom in SnO_2−graphite composite was found to be

Received: February 18, 2011
Published: May 27, 2011

more effective among various strategies to improve the conductivity and electrochemical reversibility.[22] SnO_2, when doped with fluoride ions, exhibited higher figures of merit (σ/α), where σ is the conductivity and α is the visible absorption coefficient, as compared to doping with Sb. Also, the F-doped SnO_2 topped the work function among the commonly used transparent conductors.[7] For most of the applications, including the batteries, higher surface area nanosized particles of SnO_2 would be required. SnO_2 is cost effective and also known to be least toxic among all other TCOs.[7]

For the preparation of the SnO_2:F powders, the sol–gel method (employing organometallic precursors), chemical vapor deposition, and spray pyrolysis techniques were reported. While,Ha et al.[18] obtained F-doped SnO_2 powders from the single-molecular precursor the fluoro(2-methylbutan-2-oxy) di-(pentan-2,4-dionato)tin complex by simple hydrolysis, Wu et al.[23] coupled hydrothermal treatment with hydrolysis to achieve better crystallinity. Similarly, Hana et al.[24] coupled the sol–gel and combustion methods to prepare F-doped SnO_2 nanopowders. Suffner et al.[25] used carrier gas DFM (difluoromethane) to dope SnO_2 nanoparticles with fluoride. Gamard et al.[26] prepared crystalline SnO_2 containing 3 mol % of fluoride starting from an organotin complex containing fluoride and other sol–gel-derived routes derived from fluorinated tin alkoxides for preparing SnO_2:F.[27] Senthilkumar et al.[28] reported fluoride-doped SnO_2 powders by the sol–gel process using $SnCl_2 \cdot 2H_2O$ and HF as the tin and fluoride sources. F-doped SnO_2 films have been fabricated by chemical vapor deposition techniques,[29] dip-coating technique,[30] spray pyrolysis,[14,31–38] and reactive RF sputtering.[39]

Synthetic procedures that are known to yield F-doped SnO_2 powders employed a tin source ($SnCl_2$ or $SnCl_4$) and fluorine source (NH_4F, CH_2F_2, and HF). If in case, a single-source precursor was used; it consisted of organotin complexes which required heat treatment, after the reactions, to get rid of the volatile organic impurities as well as to improve crystallinity. Total elimination of carbon impurities was found to be difficult, thus making it difficult to understand the effects of F-doping on the properties of SnO_2. In any case, doping a higher concentration of fluoride ions in SnO_2 was not easily achievable in the powder form; in many instances it is restricted by either the fluoride concentration in the starting precursor or contamination of the final product due to incomplete removal of the fluorinating agents.

Higher doping concentrations of fluoride ions have previously been reported only in thin films.[31,34,35,37,38] Higher concentrations of fluoride ions in SnO_2 are known to decrease the sheet resistance as well as increase carrier concentrations.[8,31,35,42] This is quite useful, especially in solar cell applications, to allow more photons in the UV region and to increase the transmittance value.[31,40] Therefore, it is worthwhile to investigate if one could increase the fluoride-ion concentration in SnO_2 powders through a low-temperature process which could pave the way for further understanding in this widely investigated system.

In the present study, we report the successful synthesis of fluoride-doped SnO_2 by a novel oxidation procedure in which the inorganic fluoride complex of Sn^{2+}, $KSnF_3$, was employed as the single-source precursor. $KSnF_3$ is air stable, easy to prepare, and easy to handle, and therefore, its controlled oxidation with H_2O_2 was carried out at 100 °C to obtain F-doped SnO_2. The choice of this precursor was highly justified from the fact that the mixed metal complex fluorides are highly hydroxyphilic due to the same size of the fluoride and hydroxide ions. Also, SnO_2 could very easily be obtained from the hydroxides of tin.[18] More importantly, the reactions were conducted at low temperatures which did not require any intricate set up or handling of hazardous fluorinating agents. The use of inorganic precursor prevented the product from inclusion of carbon, which is usually the contaminant starting with an organotin precursor. F-doped SnO_2 was characterized by various characterization techniques; the structure, symmetry, and size of the crystals were determined from powder X-ray diffraction, FT-IR spectrum, Raman spectroscopy, HRTEM observations, diffuse reflectance, and photoluminescence spectroscopy. The chemical composition was analyzed by X-ray photoelectron spectroscopy (XPS). The thermal stability together with evolved gas analysis was carried out to examine the suitability of the doped oxides for large-scale coatings. Additionally, the photocatalytic properties of SnO_2:F were evaluated in terms of aqueous Rh B dye degradation and realized it to be a highly efficient catalyst. The BET surface area and EPR spectroscopy techniques were employed to arrive at a conclusive proof for the presence of singly ionized oxygen vacancies on F doping in SnO_2.

2. EXPERIMENTAL METHOD

2.1. Synthesis. Our research group has reported green synthetic approaches for various mixed metal fluoride complexes.[43] $KSnF_3$ was synthesized from $SnCl_2 \cdot 2H_2O$ (99.9%, Aldrich) and KF (99%, AR grade, CDH) in a 1:3 molar ratio. In a typical procedure, 1.128 g of $SnCl_2 \cdot 2H_2O$ and 0.8715 g of KF were mixed in methanol under constant stirring and kept stirring for 2 h continuously. A white-colored powder, resulting after reaction, was separated by filtration and washed several times with distilled water. Washing with distilled water was continued until the filtrate showed the absence of any milky textured precipitate with $AgNO_3$ solution, confirming complete removal of KCl, the salt eliminated in the reaction. A white-colored suspension was obtained through the controlled oxidation procedure in which 0.2 g of $KSnF_3$ was refluxed in a mixture of 20 mL of 30% H_2O_2 and 80 mL of CH_3OH for 8 h at 100 °C. Use of methanol is to control the rate of oxidation by H_2O_2, and the product was separated by centrifugation and dried naturally over a desiccant.

2.2. Characterization. The powder X-ray diffraction patterns were recorded using a high-resolution D8 Discover Bruker X-ray diffractometer, equipped with a point detector (scintillation counter), employing monochromatized Cu $K\alpha_1$ radiation obtained through a gobel mirror with a scan rate of 1.0 s/step and step size of 0.02° at 298 K over the range of $2\theta = 10-60°$. Diffuse reflectance spectra (DRS) of the samples were recorded on Perkin- Elmer UV–vis spectrophotometer Lambda-35. In the DRS, $BaSO_4$ was used as the reference. The FT-IR spectra were recorded using a Perkin-Elmer 2000 Fourier-transform infrared (FTIR) spectrometer using KBr disks. The photoluminescence measurements were performed using a Cary Eclipse fluorescence spectrophotometer (Varian make) at room temperature employing a CW Xenon lamp source. XPS measurements were accomplished with a Perkin-Elmer series XPS using an Al K_α X-ray line (1486.6 eV) for photoelectron excitation at a base pressure of 2×10^{-9} Torr at a power of 100 w (25 mA, 15 kV). The TEM image and EDX measurements were carried out on a Philips Tecnai G^2 30 transmission electron microscope with 300 kV accelerating voltage. The SEM micrograph of the sample was recorded on a Hitachi S-3700 M microscope. Raman spectrum was obtained using a Renishaw via a microscope system with an Ar^+ laser (λ = 514.5 nm). Brunauer–Emmett–Teller (BET) surface area of the samples was obtained from physical adsorption of N_2 at 77 K using a Belsorp-Max and Belsorp-Aqua Porosimeter. Electron paramagnetic resonance (EPR) spectra were recorded with a JEOL JES-FE3XG electron spin resonance spectrometer. The EPR spectra were calibrated with diphenylpicrylhydrazyl, DPPH ($g = 2.0037$). Thermogravimetry (TG) and derivative thermogravimetry (DTG) analyses coupled with mass spectrometry were obtained using the Pyris 1 TGA in the range 50−400 °C under helium at a flow rate 50 mL min^{-1} and at a heating rate of 5 °C min^{-1}, using a Perkin Elmer Clarus mass spectrometer. In the experiments, the powder samples were placed in platinum crucibles and the electron impact mass spectra (70 eV) were continuously recorded with scans from 10 to 500 amu.

2.3. Photocatalytic Experiments. Photocatalytic studies under UV ($\lambda < 400$ nm) light were carried out in an immersion-type, in-house fabricated photochemical reactor. A double-lined quartz tube with dimensions of 3 cm i.d., 4 cm o.d., and 17 cm length was placed in an outer pyrex glass reactor of 7.5 cm i.d. and 18 cm length. A high-pressure mercury vapor lamp of 125 W (Philips, India) was placed inside the quartz tube. The outer shell of this fluorescent lamp was removed in order to have maximum intensity, and the emission profile of the lamp is shown in the Supporting Information.[44] Water circulation was carried out through the quartz tube so as to avoid any thermal effects and to serve as well as an IR filter. All experiments were conducted at room temperature. The appropriate dye solution, to be decomposed, was taken along with the required amount of catalyst in the outer pyrex container and was constantly stirred to maintain a homogeneous suspension. The solar intensity was measured at regular intervals using a pyranometer, which yielded an average value of 3.39 μW cm^{-1}.[45] The dye was dissolved in doubly distilled water. A typical experiment of degradation was carried out as follows: 0.1 g of the catalyst was added to 100 mL of aqueous solution of Rh B with an initial concentration of 5×10^{-6} mol/L for irradiation experiments. Prior to irradiation, the suspension of the catalyst and dye solution was stirred in the dark for 1 h to reach the equilibrium adsorption. Five milliliter aliquots were pipetted out periodically from the reaction mixture. The solutions were centrifuged, and the concentration of the solutions was determined by measuring the maximum absorbance ($\lambda_{max} = 552$ nm).

3. RESULTS AND DISCUSSION

3.1. Structural and Morphological Studies. Monoclinic $KSnF_3$ was synthesized by a simple and green precipitation reaction of $SnCl_2 \cdot 2H_2O$ and KF in methanol as reported for other KMF_3 fluoride complexes.[43] The powder X-ray diffraction pattern of $KSnF_3$ is presented in Figure 1a, which matched well with JCPDS file no. 16-0794. The powder X-ray diffraction pattern of the product from reaction of $KSnF_3$ with H_2O_2 (shown in Figure 1b) suggested formation of rutile-structured SnO_2 having tetragonal symmetry with peak positions and intensities matching well with JCPDS file no. 41-1445. The Le-Bail fit[46] of the powder X-ray diffraction pattern of the SnO_2:F (inset of Figure 1) yielded the lattice constants $a = 4.7106$ (1) Å and $c = 3.1970$ (1) Å, matching well with the reported values. SnO_2 was also generated by reacting $SnCl_2 \cdot 2H_2O$ with H_2O_2 for the purpose of comparison, and its powder X-ray diffraction pattern is shown in Figure 1c. Broadening of the diffracted peaks, signifying the low crystallite size of the products, was quite evident in the SnO_2 obtained from both $SnCl_2 \cdot 2H_2O$ as well as $KSnF_3$. The average crystallite size, as verified from the Scherrer analysis, was less than 3 nm. Insertion of fluoride ion in SnO_2 was not quite evident from the powder X-ray diffraction patterns wherein the broadness of the peaks masked any small shifts with respect to SnO_2 obtained from $SnCl_2 \cdot 2H_2O$.

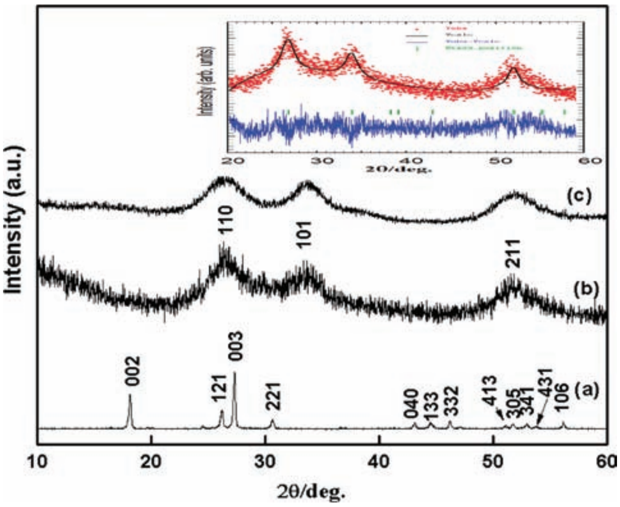

Figure 1. PXRD pattern of (a) $KSnF_3$, (b) oxidized product from $KSnF_3$, and (c) SnO_2 from $SnCl_2 \cdot 2H_2O$. (Inset) Le-Bail fit of the powder X-ray diffraction pattern of oxidized product from $KSnF_3$.

A plate-like morphology was observed in the SEM micrographs (Figure S1, Supporting Information). Agglomeration of particles, due to high surface forces, such as van der Waals and capillary forces, was observed in the TEM images (Figure 2).[47] The results of crystallite size measurements from TEM images were in good agreement with the Scherrer analysis. While spot-wise EDX analysis of the SEM and TEM images indicated the presence of fluoride in the SnO_2 lattice (Supporting Information, Figure S2), further quantification was obtained from high-resolution XPS analysis.

Figure 3 shows the high-resolution survey XPS spectrum of the SnO_2:F, and to compensate for surface charging effects, binding energies were calibrated using the C 1s hydrocarbon peak at 284.6 eV. The binding energies of Sn $3d_{5/2}$, O 1s, and F 1s were located at 487.4, 531.87, and 685.08 eV, respectively. Sn $3d_{5/2}$ peak showed the Sn^{4+} bonding state as observed earlier in SnO_2[48] and SnF_4.[49,50] This also indicated that Sn−F bonding formed in the SnO_2 framework, which was further supported by the FTIR spectrum (discussed later in this section). These observations pointed out the absence of potassium ion in the oxidized product. The core level F 1s spectrum observed at 685.08 eV (inset of Figure 3) was fitted in the Gaussian profile, confirming the doping of fluoride in the SnO_2 lattice. The concentration of the constituent elements was obtained using the following relationship

$$C_x = \frac{\frac{A_x}{SF_x}}{\sum_x^N \frac{A_x}{SF_x}} \times 100$$

where A_x is the area under the curve for element x and SF_x is the corresponding sensitivity factor. On this basis, the concentration of the tin ions, oxide ions, and fluoride ions was 33.27%, 45.50%, and 21.23%, respectively. The EDX measurements from SEM and TEM images also yielded the dopant concentration in the same range (Figure S2, Supporting Information). Such a high concentration of F^- ion in SnO_2 has earlier been reported only in thin films.[31,34,35,37,38]

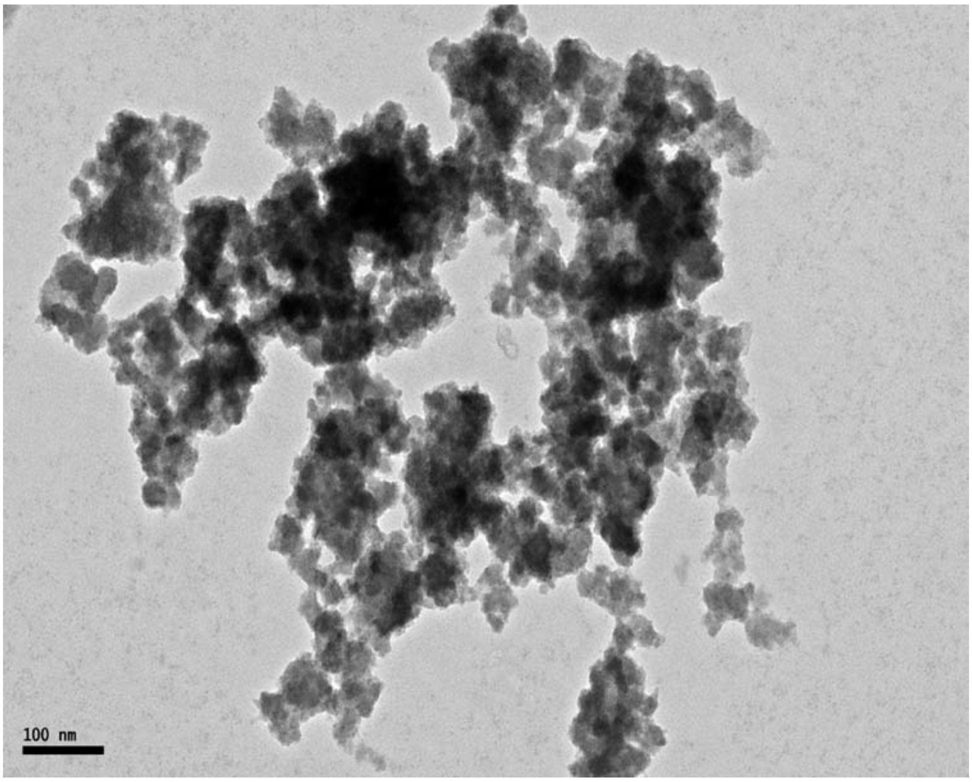

Figure 2. TEM image of SnO_2:F.

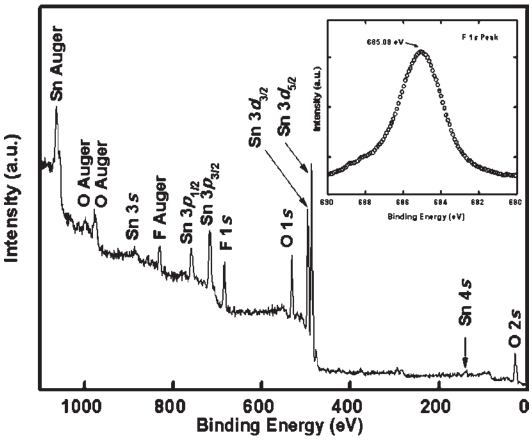

Figure 3. Survey XPS spectrum of fluoride-doped SnO_2. The core level spectrum of F 1s is shown in the inset.

The following mechanism, involving the sequences of chemical reactions, could be conceived for the formation of inherently F-doped SnO_2

$$KSnF_3 + H_2O_2 \rightarrow KSnF_{3-x}(OH)_x$$

$$KSnF_{3-x}(OH)_x \rightarrow Sn(OH)_4 + HF + KOH$$

$$Sn(OH)_4 + HF \rightarrow SnO_2\text{: F}$$

H_2O_2, being a powerful oxidizing agent, dissociated the complex fluoride while simultaneously oxidizing Sn^{2+} to Sn^{4+}, resulting probably in $Sn(OH)_4$ and HF. Highly reactive HF, presumed to be generated in situ, might lead to doping of some of the hydroxyl groups with F^-.

The thermal stability of this heavily F-doped SnO_2 system was examined by the hyphenated TG-MS techniques. This technique is quite useful to understand the species evolved during heating and could reveal the feasibility of the use of F-doped SnO_2 nanoparticles for coating films, especially by the spray pyrolysis technique. As mentioned earlier, this is the most commonly employed method for the SnO_2 system. It is important to recognize that the evolution of HF vapors and F_2 during the spray pyrolysis technique must be prevented due to their hazardous nature. Often, this information has not been included in the research publications as claimed by Gamard et al.[27] The plot of time versus mass loss for the SnO_2:F system is presented in Figure 4 at a heating rate of 5 °C/min. The evolved gas analysis was carried out by mass spectrometry at periodic intervals of time. The analysis of mass spectrometric data of the gases evolved on heating SnO_2:F at 70, 110, 125, 250, 310, and 370 °C is presented in Table 1. The corresponding plots are provided in the Supporting Information (Figures S3–S5). Evolution of an appreciable amount of HF in the evolved gases was observed only above 300 °C, suggesting that the powders obtained in the present study have fair thermal stability. This finding would be quite significant for making large area coatings by the spray pyrolysis technique, which employs temperatures of the same order for deposition.

The FTIR spectrum of SnO_2 has been demonstrated to be a good indicator for detecting the increased disorder nature of its rutile structure, especially when doped with fluoride ions.[39,51] Selected regions of the FT-IR spectra of SnO_2 and SnO_2:F powders are shown in Figure 5A. The FT-IR spectrum of SnO_2, from $SnCl_2 \cdot 2H_2O$, showed bands at 547 and 664 cm^{-1} which

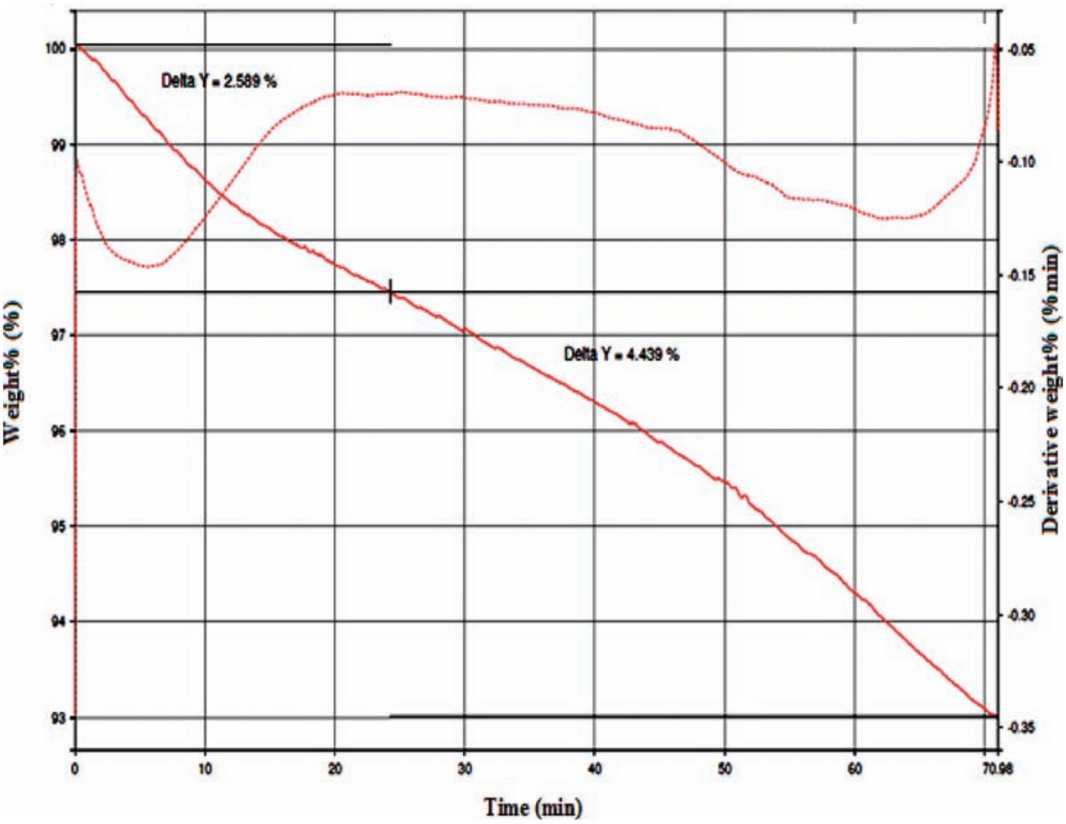

Figure 4. Thermogravimetry trace of SnO_2:F.

Table 1. TGA Coupled with MS Data for SnO_2:F

pyrolysis steps	sampling temperature (°C)	mass loss intensity (%)	species detected
1	70	0.3	H_2O, F, HF,OH
2	110	1.3	F, O_2, CO_2
3	125	0.3	H_2O, F, HF, N_2, O_2, OH
4	250	1.7	
5	310	1.1	CO_2, HF
6	370	1.6	CO_2, HF

were assigned to Sn−O and O−Sn−O stretching vibrations, respectively. The FTIR spectrum of SnO_2:F showed bands at 482, 586, 642, and 740 cm^{-1} (Figure 5A). Bands at 586 and 642 were assigned to Sn−O and Sn−O−Sn stretching vibrations, respectively.[28,52] The disappearance and weakening of the intensity of the vibrational band at 642 cm^{-1} were observed as inclusion of fluoride in SnO_2 occurred; the other characteristic feature was the presence of Sn−F vibration modes. This feature was essentially observed only at higher doping levels, thereby causing splitting of the band due to O−Sn−O.[39] It could effectively be argued that the doping of fluoride ions resulted in oxygen vacancies, thereby increasing the electropositive character around the Sn−O_{Vac} bond. In such a scenario, the additional occupations of fluoride ions for some oxygen vacancies were certainly possible in the lattice. It can be suggested that at low doping levels fluoride ions prefer to occupy oxide positions in the SnO_2 lattice. After reaching a threshold concentration, additional doping could allow the fluoride ions to occupy the interstitial positions, producing a negative effect on the carrier concentration which in turn affected the infrared reflectivity of SnO_2 powder. The presence of interstitial fluorine atoms also would increase the lattice disorder remarkably, resulting in the shift of vibration frequency of the Sn−O bond in the FT-IR spectrum.[38]

In general, a shift in the peak positions accompanied with broadening of the Raman bands were observed for nanoparticles with a size of less than 7 nm.[53,54] The room-temperature Raman spectrum of the SnO_2:F nanocrystals showed bands at 455, 588, and 874 cm^{-1} (Figure 5B). Rutile-structured SnO_2 belongs to the space group D^{14}_{4h}, of which the normal lattice vibration mode on the basis of group theory is given as[55]

$$\Gamma = 1A_{1g} + 1A_{2g} + 1A_{2u} + 1B_{1g} + 1B_{2g} + 2B_{1u} + 1E_g + 3E_u$$

Among these, B_{1g}, E_g, A_{1g}, and B_{2g} are the active Raman modes. Consequently, three fundamental Raman peaks at 477, 636, and 777 cm^{-1}, corresponding to the E_g, A_{1g}, and B_{2g} vibration modes, respectively, were observed, conforming with earlier reports (Figure 5B).[56] Bands at 626 and 776 cm^{-1} further confirmed that the pure SnO_2 nanocrystals (from $SnCl_2 \cdot 2H_2O$) possessed the tetragonal symmetry of the rutile structure. A downward shift of the A_{1g} and B_{2g} vibration modes was observed for the fluoride-doped SnO_2 nanocrystals (Figure 5B). This could arise due to the crystallite size reduction.[53] In addition to the fundamental Raman peaks of rutile SnO_2, weak bands at around 326 cm^{-1} were also observed in SnO_2:F.[57] Also, as a consequence of disorder activation of oxygen vacancies, a band at 576 cm^{-1} appeared.[58] The band at 446 cm^{-1} observed for pure SnO_2

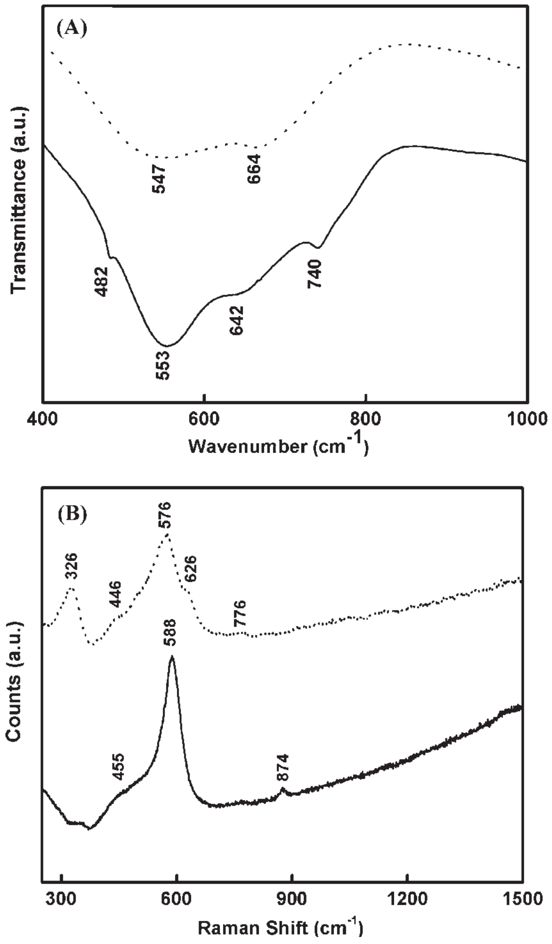

Figure 5. (A) FTIR spectra of SnO_2 (dotted line) and SnO_2:F (solid line). (B) Raman spectrum of SnO_2 (dotted line) and SnO_2:F (solid line).

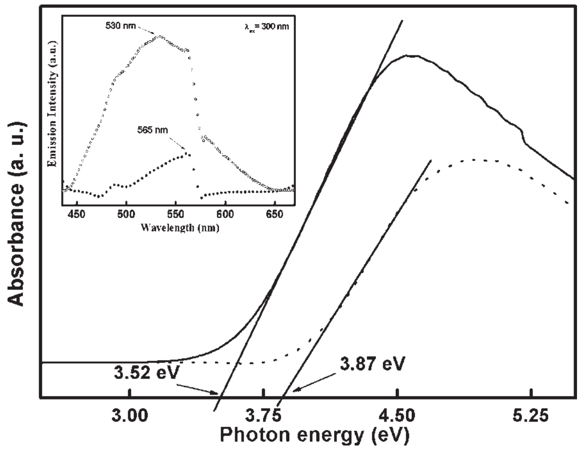

Figure 6. Plot of absorbance versus photon energy of SnO_2 (solid line) and SnO_2:F (dotted line). (Inset) Photoluminescence spectrum of SnO_2 (filled cirles) and SnO_2:F (open circles).

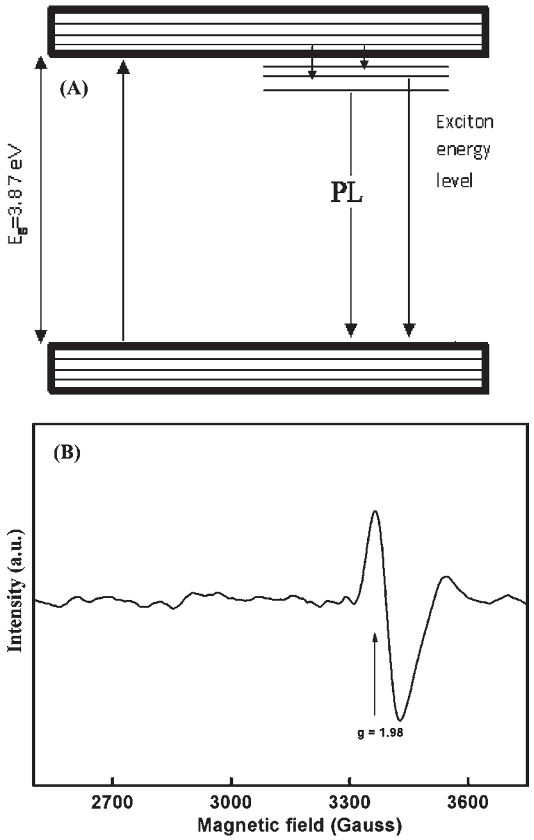

Figure 7. (A) Schematic diagram for the excitation and relaxation processes leading to the photoluminescence. (B) ESR spectrum of SnO_2:F at room temperature.

nanocrystals could be assigned to the bending mode of Sn−O−Sn.[59] According to the phonon confinement model,[53,60] both the long-range order and the entire translational symmetry get destroyed due to the effect of three-dimensional confinement of nanoparticles, which would result in the variation of the lattice vibration mode. The phonon wave function could be described by using the wave packet that is confined within the nanoparticles instead of a plane. Peak broadening in the Raman spectrum might be the result of a random distribution of nanosized crystallites. A base line shift with an increase in wavenumber was observed in the Raman spectrum of the fluoride-doped SnO_2, suggesting its fluorescent nature.

3.2. Optical Properties. The diffuse reflectance spectra of the F-doped and synthesized SnO_2 exhibited a significant change in their absorption behavior. Very strong quantum confinement effects of heavily doped nanocrystals leading to unusual electronic and optical properties are not yet completely understood. This statement gained strong support from the very recent work of Mocatta et al.[41] in which heavy doping in *p*- or *n*-type semiconductor nanocrystals resulted in the confined impurity band and band tailing leading to a strong blue shift. A blue shift of the exciton absorption was observed from 3.52 to 3.87 eV (calculated by the Kubelka−Munk function) in the SnO_2 system on F doping. This can only be explained by the Moss−Burstein effect in which the excessive F doping into the n-type SnO_2 lattice could possibly have led to the increased band filling by the donated electrons (Figure 6).[40,41,61] This observation validated the results of Mocatta et al.[41] observed for III−V semiconductors.

The photoluminescence (PL) spectrum (inset of Figure 6) of the SnO_2:F nanocrystals exhibits broad visible light emission with the maximum centering at 506 nm. This PL emission can be considered to be an excitonic PL process in which the nonradiative transitions of the electrons excited from the conduction

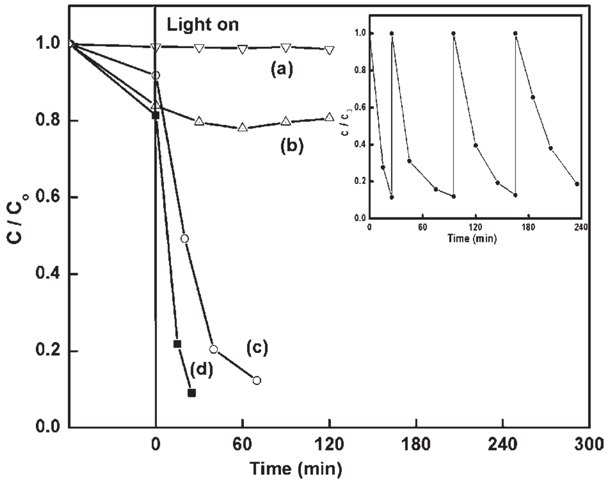

Figure 8. (a) Photolysis of RhB under UV irradiation. Photolysis (b) in the dark, (c) in the presence of SnO_2 (from $SnCl_2 \cdot 2H_2O$), and (d) in the presence of SnO_2:F over 5 μM Rh B under 125 UV light. (Inset) Repeated photodegradation of Rh B solution by SnO_2:F.

band (CB) bottom to different sub-bands (or surface states) occur first followed by subsequent radiative transitions from the sub-band to the top of the valence band (VB) occurring as depicted schematically in Figure 7A.[62] The intense PL emission could be the result of the defects created as a result of F-doping and due to the inherent defects occurring during lattice formation. The oxygen vacancies resulting from the doping could possibly interact with some of the interstitial vacancies, leading to formation of a considerable amount of trapped states within the band gap, resulting in intense PL emission.[62] The blue shift observed on F doping in SnO_2 in the absorption measurements was confirmed in the PL spectra as well. By both the absorption and the photoluminescence measurements, a blue shift of the exciton absorption due to the Moss–Burstein effect was confirmed.[40,41,61] A diminishing singly ionized oxygen vacancy could possibly have resulted in the prominent green emission in the PL spectrum. Our results suggested that oxygen vacancies played a critical role in the observed green emission of SnO_2:F. Evidence for the singly ionized oxygen vacancies was obtained from the presence of an ESR signal with $g = 1.98$ for the F-doped SnO_2 (Figure 7B). Additionally, a very weak feature with a lower g value was seen in the ESR spectrum, the origin of which is not clear at present. Such observations have been reported earlier in ZnO and SnO_2 samples,[63,57] and ours is the first report on F-doped SnO_2 giving rise to a green emission caused by the singly ionized oxygen vacancies.

3.3. Photocatalytic Studies. The photocatalytic activity of SnO_2:F was evaluated by photocatalytic decolorization of the aqueous solution of the dye Rh B at room temperature under UV irradiation (Figure 8). Repeated decomposition of Rh B under UV radiation by SnO_2:F is shown in the inset of Figure 8, indicating that the catalyst was active and chemically stable toward successive cycles of photodecomposition. The maximum absorbance for the aqueous RhB dye was observed at around 552 nm. In the presence of SnO_2:F as the catalyst, the absorbance decreased initially, indicating adsorption of the dye Rh B (in the dark). Further, a substantial decrease in the absorbance of Rh B was observed after conducting the reaction under UV light irradiation. The solution turned colorless within 20 min of irradiation. Similar experiments were carried out for the pure SnO_2 nanocrystals as well. From these experiments, the variation in the concentrations of the Rh B solutions was plotted against the time (Figure 8). These results clearly demonstrated that SnO_2:F mineralized Rh B faster than synthesized SnO_2 under similar experimental conditions.

Table 2. BET Surface Area, Mean Pore Diameter, and Total Pore Volume of SnO_2:F and SnO_2

compound	BET surface area (m^2/g)	mean pore diameter (nm)	total pore volume (cm^3/g)
SnO_2:F	45.16	13.97	0.1578
pure SnO_2	207.81	1.97	0.1023

To gain more insight into the factors contributing to the photocatalytic properties of nanosized SnO_2:F, the specific surface area, pore size, and pore volumes of the SnO_2 and SnO_2:F nanocrystals were measured by the BET method by N_2 adsorption and desorption at 77 K, and the results are tabulated in Table 2. The corresponding adsorption–desorption isotherms are shown in Supporting Information Figure S6. While the BET surface area of SnO_2:F was 45.16 m^2/g, undoped SnO_2 possessed a surface area of 207.81 m^2/g. Although, the surface area of SnO_2:F is smaller than pure SnO_2, the photocatalytic response of the former is higher as compared to the latter. This was attributed to higher oxygen vacancies in SnO_2:F, induced by the heavy fluoride ion doping. The presence of a higher concentration of oxygen vacancies was further supported by the broadness of the photoemission spectrum under excitation with $\lambda = 300$ nm (inset of Figure 6). Though one could not directly derive any correlation between the intensity of the emission in the PL spectrum and the photocatalytic activity in excitonic oxide semiconductors, the suggestion of Liqiang et al.[64] in which a possible intense PL emission could possibly result in higher photocatalytic activity due to the higher concentration of oxygen vacancies offered a satisfying explanation for our observation. The specific surface area and average pore volume of 45 m^2/g and 0.157 cm^3/g for SnO_2:F, measured in the present study, were very close to those of commercial photocatalyst Degussa P25 (50 m^2/g and 0.16 cm^3/g, respectively).[65] Since, the dye pollutants generally were adsorbed onto the active sites of the catalysts, the higher surface area and larger pore size would certainly allowed rapid diffusion of various reactants and products during the photocatalytic reactions, thereby accelerating the entire photodegradation reaction.[66] The pseudo-first-order rate constant for decomposition of Rh B over SnO_2:F was 8.77×10^{-2} min^{-1}. The powder X-ray diffraction pattern of SnO_2:F after photocatalytic degradation showed the structure to be intact, indicating that there was no reaction between the organic dye (Rh B) and the photocatalyst (Supporting Information, Figure S8).

4. CONCLUSIONS

Air-stable $KSnF_3$ has been successfully demonstrated to be an ideal single-source precursor for producing fluoride-ion-doped SnO_2 nanocrystals at low temperatures. FTIR and Raman spectroscopic analysis of the SnO_2:F indicated the presence of a very high concentration and disordered nature of oxygen vacancies and the possible presence of fluoride ions in the interstitials in addition to the designated oxygen positions in the rutile lattice. XPS analysis revealed a fluoride concentration of 21.23% in SnO_2, the highest until now, achieved in powders.

The enormous blue shift observed in the F-doped SnO_2 nanocrystals was attributed to the overdoped situation with increased carrier concentration. This system offered another example in which the Moss−Burstein effect has manifested in interesting optoelectronic properties. A broad green emission observed in the PL spectrum of SnO_2:F also resulted from the singly ionized oxygen vacancies caused by heavy fluoride-ion doping. An ESR signal with a g value of 1.98 provided conclusive evidence for the singly ionized vacancies in this system. Evaluation of SnO_2:F as a photocatalyst for degradation of aqueous RhB dye solutions revealed it to be a promising photocatalyst. The present procedure eliminated the requirement of intricate experimental setup as well as the use of hazardous fluorinating agents usually employed for doping fluoride ions and resulted in nanosized powders which can effectively be suspended in suitable medium for large-scale coatings by dip coating, electrophoretic, or spray pyrolysis procedures for thin film fabrication.

■ ASSOCIATED CONTENT

Ⓢ Supporting Information. SEM image of SnO_2:F, EDX of SnO_2:F from SEM and TEM analysis, mass spectral details of evolved gases after heating SnO_2:F at 70, 110, 125, 250, 310, and 370 °C, nitrogen adsoption−desorption isotherms of SnO_2 and SnO_2:F, emission spectrum of a 125 W mercury vapor pressure (Philips) lamp, and powder X-ray diffraction pattern of SnO_2:F before and after photocatalytic experiments. This material is available free of charge via the Internet at http://pubs.acs.org.

■ AUTHOR INFORMATION

Corresponding Author

*E-mail: rnagarajan@chemistry.du.ac.in.

■ ACKNOWLEDGMENT

The authors sincerely thank and acknowledge DST (Nanomission), Government of India for the financial support to carry out this work. The authors thank Dr. S. Uma for many useful discussions. One of the authors, V.K., wishes to record his sincere thanks to UGC, Government of India for a JRF fellowship. The authors also thank Miss Sudha (DCE, University of Delhi) for providing SEM-EDX facilities and Mr. Surender Kumar for help in PL measurements. Thanks to Manish Kumar and Vipin Kumar of USIC for helping us with PXRD and EPR measurements. Timely help and support from Perkin-Elmer, India for the TG-MS data on our samples is gratefully acknowledged.

■ REFERENCES

(1) Smith, A. M.; Nie, S. *Acc. Chem. Res.* **2010**, *43*, 190.

(2) Alivisatos, A. P. *Science* **1996**, *271*, 933.

(3) Alivisatos, A. P. *J. Phys. Chem.* **1996**, *100*, 13226.

(4) Pan, Z. W.; Dai, Z. R.; Wang, Z. L. *Science* **2001**, *291*, 1947.

(5) Feng, X.; Sayle, D. C.; Wang, Z. L.; Paras, M. S.; Santora, B.; Sutorik, A. C.; Sayle, T. X. T.; Yang, Y.; Ding, Y.; Wang, X.; Her, Y.-S. *Science* **2006**, *312*, 1504. zum Felde, U.; Haase, M.; Weller, H. *J. Phys. Chem. B* **2000**, *104*, 9388.

(6) Wang, F.; Han, Y.; Lim, C. S.; Lu, Y.; Wang, J.; Xu, J.; Chen, H.; Zhang, C.; Hong, M.; Liu, X. *Nature* **2010**, *463*, 1061.

(7) Gordon, R. G. *MRS Bull.* **2000**, 52.

(8) Chopra, K. L.; Major, S.; Pandya, D. K. *Thin Solid Films* **1983**, *102*, 1.

(9) Han, C.-H.; Han, S.-D.; Singh, I.; Toupance, T. *Sens. Actuators B* **2005**, *109*, 264.

(10) D' Arienzo, M.; Armelao, L.; Cacciamani, A.; Mari, C. M.; Polizzi, S.; Ruffo, R.; Scotti, R.; Testino, A.; Wahba, L.; Morazzoni, F. *Chem. Mater.* **2010**, *22*, 4083.

(11) Colvin, V. L.; Schlamp, M. C.; Alivisatos, A. P. *Nature* **1994**, *370*, 354.

(12) Vlasov, Y. A.; Yao, N.; Norris, D. J. *Adv. Mater.* **1999**, *11*, 165.

(13) Norris, D. J.; Yao, N.; Charnock, F. T.; Kennedy, T. A. *Nano Lett.* **2001**, *1*, 3.

(14) Frank, G.; Kauer, E.; Kostlin, H.; Schmitte, F. J. *Sol. Energy Mater.* **1983**, *8*, 387.

(15) Linsebigler, A. L.; Lu, G.; Yates, J. T. *Chem. Rev.* **1995**, *95*, 735. Hoffmann, M. R.; Martin, S. T.; Choi, W.; Bahnemann, D. W. *Chem. Rev.* **1995**, *95*, 69. Al-Ekabi, H.; Serpone, N.; Pelizzetti, E.; Minero, C.; Fox, M. A.; Draper, R. B. *Langmuir* **1989**, *5*, 250.

(16) Zhao, G.; Cui, X.; Liu, M.; Li, P.; Zhang, Y. G.; Cao, T. C.; Li, H.; Lei, Y; Liu, L.; Li, D. *Environ. Sci. Technol.* **2009**, *43*, 1480. Velikokhatnyi, O. I.; Kumta, P. N. *Physica B* **2011**, *406*, 471.

(17) Wang, Y.; Djerdj, I.; Smarsly, B.; Antonietti, M. *Chem. Mater.* **2009**, *21*, 3202.

(18) Archer, P. I.; Radovanovic, P. V.; Heald, S. M.; Gamelin, D. R. *J. Am. Chem. Soc.* **2005**, *127*, 14479.

(19) Ha, H.-W.; Kim, K.; Borniol, M.; Toupance, T. *J. Solid State Chem.* **2006**, *179*, 702.

(20) James, A. C. W. P.; Zahurak, S. M.; Murphy, D. W. *Nature* **1989**, *338*, 240. Rao, C. N. R.; Raveau, B. *Acc. Chem. Res.* **1989**, *22*, 106. Cava, R. J. *Science* **1990**, *247*, 656.

(21) Varghese, O. K.; Malhotra, L. K. *Sens. Actuators B* **1998**, *53*, 19. Ferrere, S.; Zaban, A.; Gregg, B. A. *J. Phys. Chem.* **1997**, *101*, 4490.

(22) Morales, J.; Sanchez, L. *J. Electrochem. Soc.* **1999**, *146*, 1640. Maruyama, T.; Tabata, K. *J. Appl. Phys.* **1990**, *68*, 4282. Ahn, J.-H.; Wang, G. X.; Yao, J.; Liu, H. K.; Dou, S. X. *J. Power Sources* **2003**, *119−121*, 45. Read, J.; Foster, D.; Wolfenstine, J.; Behl, W. *J. Power Sources* **2001**, *96*, 277. Bruneaux, J.; Cachet, H.; Froment, M.; Messad, A. *Electrochim. Acta* **1994**, *39*, 1251. Kwon, C. W.; Campet, G.; Portier, J.; Poquet, A.; Fournes, L.; Labrugere, C.; Jousseaume, B.; Toupance, T.; Choy, J. H.; Subramanian, M. A. *Int. J. Inorg. Mater.* **2001**, *3*, 211.

(23) Wu, S.; Yuan, S.; Shi, L.; Zhao, Y.; Fang, J. *J. Colloid Interface Sci.* **2010**, *346*, 12.

(24) Han, C.-H.; Han, S.-D.; Gwak, J.; Khatkar, S. P. *Mater. Lett.* **2007**, *61*, 1701.

(25) Suffner, J.; Agoston, P.; Kling, J.; Hahn, H. *J. Nanopart. Res.* **2010**, *12*, 2579.

(26) Gamard, A.; Jousseaume, B.; Toupance, T.; Campet, G. *Inorg. Chem.* **1999**, *38*, 4671.

(27) Boegeat, D.; Jousseaume, B.; Toupance, T.; Campet, G.; Fournes, L. *Inorg. Chem.* **2000**, *39*, 3924. Franc, C.; Jousseaume, B.; Linker, M.; Toupance, T. *Chem. Mater.* **2000**, *12*, 3100. Gamard, A.; Babot, O.; Jousseaume, B.; Rascle, M.-C.; Toupance, T.; Campet, G. *Chem. Mater.* **2000**, *12*, 3419.

(28) Senthilkumar, V.; Vickraman, P.; Ravikumar, R. *J. Sol-Gel Sci. Technol.* **2010**, *53*, 316.

(29) Ray, S. C.; Karanjai, M. K.; DasGupta, D. *Thin Solid Films* **1997**, *307*, 221.

(30) Ray, S. C.; Karanjai, M. K.; DasGupta, D. *Surf. Coat. Technol.* **1998**, *102*, 73.

(31) Shanthi, E.; Banerjee, A.; Dutta, V.; Chopra, K. L. *J. Appl. Phys.* **1982**, *53*, 1615.

(32) Yadav, A. A.; Masumdar, E. U.; Moholkar, A. V.; Spallart, M. N.; Rajpure, K. Y.; Bhosale, V. H. *J. Alloys Compd.* **2009**, *488*, 350.

(33) Memarian, N.; Rozati, S. M.; Elamurugu, E.; Fortunato, E. *Phys. Status Solidi C* **2010**, *9*, 2277.

(34) Zhang, B.; Tian, Y.; Cai, W. *Mater. Lett.* **2010**, *64*, 2707.

(35) Miao, D.; Zhao, Q.; Wu, S.; Wang, Z.; Zhang, X.; Zhao, X. *J. Non-Cryst. Solids* **2010**, *356*, 2557.

(36) Adnane, M.; Cachet, H.; Folcher, G.; Hamzaoui, S. *Thin Solid Films* **2005**, *492*, 240.

(37) Acosta, D. R.; Zirconi, E. P.; Montoya, E.; Estrada, W. *Thin Solid Films* **1996**, *288*, 1.

(38) Zhang, B.; Tian, Y.; Zhang, J. X.; Cai, W. *J. Mater. Sci.* **2011**, *46*, 1884.

(39) Czapla, A.; Kusior, E.; Bucko, M. *Thin Solid Films* **1989**, *182*, 15.

(40) Liang, H.; Gordon, R. G. *J. Mater. Sci.* **2007**, *42*, 6388.

(41) Mocatta, D.; Cohen, G.; Schattner, J.; Millo, O.; Rabani, E.; Babin, U *Science* **2011**, *332*, 77. Abram, A.; Rees, G. J.; Wilson, B. L. H. *Adv. Phys.* **1978**, *27*, 799.

(42) Elangovan, E.; Ramamurthi, K. *Appl. Surf. Sci.* **2005**, *249*, 183.

(43) Tyagi, N.; Reddy, A. A.; Nagarajan, R. *Opt. Mater.* **2010**, *33*, 42. Tyagi, N.; Ghanti, E.; Gupta, N.; Lalla, N. P.; Nagarajan, R. *Bull. Mater. Sci.* **2009**, *32*, 583.

(44) Msscientific Chromatographie-Handel GmbH Gneisenaustrasse 66/67, 10961 Berlin, Germany.

(45) Priya, M. H.; Madras, G. *Ind. Eng. Chem. Res.* **2006**, *45*, 482.

(46) Bail, A. L.; Duroy, H.; Fourquet, J. L. *Mater. Res. Bull.* **1988**, *23*, 447.Carvajal, J. R. Full Prof Suite Program (version 1.00), February 2007, Laboratoire Leon, Brillouin (CEA/CNRS): CEA-Saclay, 91191, Gifsur-Yvette, Cedex, France.

(47) Pugh, R. J.; Bergstrom, L. *Surface and colloid chemistry in advanced ceramic processing*; Marcel Dekker: New York, 1994; p 273.

(48) Zhi, X.; Zhao, G.; Zhu, T.; Li, Y. *Surf. Interface Anal.* **2008**, *40*, 67.

(49) Morgan, W. E.; Wazer, J. R. V. *J. Phys. Chem.* **1973**, *77*, 964.

(50) Grutsch, P. A.; Zeller, M. V.; Fehlner, T. P. *Inorg. Chem.* **1973**, *6*, 1431.

(51) Zhang, B.; Tian, Y.; Zhang, J. X.; Cai, W. *Appl. Phys. Lett.* **2011**, *98*, 021906.

(52) Xiong, H.-M.; Zhao, K.-K.; Zhao, X.; Wang, Y.-W.; Chen, J.-S. *Solid State Ionics* **2003**, *159*, 89.

(53) Campbell, I. H.; Fauchet, P. M. *Solid State Commun.* **1986**, *58*, 739.

(54) Zheng, M. J.; Ma, L.; Xu, W. L.; Ding, G. Q.; Shen, W. Z. *Appl. Phys. A: Mater. Sci. Proc.* **2005**, *81*, 721.

(55) Porto, S. P. S.; Fleury, P. A.; Damen, T. C. *Phys. Rev.* **1967**, *154*, 522.

(56) Park, M.-S.; Wang, G.-X.; Kang, Y.-M.; Wexler, D.; Dou, S.-X.; Liu, H.-K. *Angew. Chem., Int. Ed.* **2007**, *46*, 750.

(57) Sun, S. H.; Meng, G. W.; Zhang, G. X.; Gao, T.; Geng, B. Y.; Zhang, L. D.; Zuo, J. *Chem. Phys. Let.* **2003**, *376*, 103.

(58) Dieguez, A.; Romano-Rodriguez, A.; Vila, A.; Morante, J. R. *J. Appl. Phys.* **2001**, *90*, 1550.

(59) Tran, T. V.; Turrell, S.; Eddafi, M.; Capoen, B.; Bouazaoui, M.; Roussel, P.; Berneschi, S.; Righini, G.; Ferrari, M.; Bhaktha, S. N. B.; Cristini, O.; Kinowski, C. *J. Mol. Struct.* **2010**, *976*, 314.

(60) Nemanich, R. J.; Solin, S. A.; Martin, R. M. *Phys. Rev. B* **1981**, *23*, 6348.

(61) Shanthi, E.; Banerjee, A.; Chopra, K. L. *Thin Solid Films* **1982**, *88*, 93.

(62) Liqiang, J.; Yichun, Q.; Baiqi, W.; Shudan, L.; Baojiang, J.; Libin, Y.; Wie, F.; Honggang, F.; Jiazhong, S. *Sol. Energy Mater.* **2006**, *90*, 1773.

(63) Vanheusden, K.; Seager, C. H.; Warren, W. L.; Tallant, D. R.; Voigt, J. A. *Appl. Phys. Lett.* **1996**, *68*, 403. Riehl, N.; Ortman, O. *Z. Elektrochem.* **1952**, *60*, 149. Kasai, P. H. *Phys. Rev.* **1963**, *130*, 989.

(64) Liqiang, J.; Xiaojun, S.; Baifu, X.; Baiqi, W.; Weimin, C.; Honggang, F. *J. Solid State Chem.* **2004**, *177*, 3375.

(65) Mao-Xiang, J.; Xue-Qin, J.; Wang-Xing, L.; Dong-Hong, L.; Zhou, W. *Micro Nanosyst.* **2009**, *1*, 12.

(66) Kim, D. S.; Han, S. J.; Kwak, S. Y. *J. Colloid Interface Sci.* **2007**, *316*, 85. Wang, Z.; Mao, L.; Lin, J. *J. Photochem. Photobiol., A: Chem.* **2001**, *77*, 261. Sakatani, Y.; Grosso, D.; Nicole, L.; Boissiere, C.; Soler-Illia, G. J. de A. A.; Sanchez, C. *J. Mater. Chem.* **2006**, *16*, 77.